Front. Earth Sci. 2024, 18(2): 324–335
https://doi.org/10.1007/s11707-022-1009-y

RESEARCH ARTICLE

Low-latitude hydroclimate changes related to paleomagnetic variations during the Holocene in coastal southern China

Tingwei ZHANG[1], Xiaoqiang YANG (✉)[1], Jian YIN[1], Qiong CHEN[2], Jianfang HU[3], Lu WANG[4], Mengshan JU[5], Qiangqiang WANG[1]

1 School of Earth Science and Engineering/Guangdong, Provincial Key Laboratory of Geodynamics and Geohazards/Southern Marine Science and Engineering Guangdong Laboratory (Zhuhai), Sun Yat-sen University, Guangzhou 510275, China
2 Institute of Cultural Heritage, Shandong University, Qingdao 266237, China
3 State Key Laboratory of Organic Geochemistry, Guangzhou Institute of Geochemistry, Chinese Academy of Sciences, Guangzhou 510640, China
4 College of Urban and Environmental Sciences, Peking University, Beijing 100871, China
5 Institute of Oceanology, Chinese Academy of Sciences, Qingdao 266071, China

Abstract The variations in precipitation have displayed a complex pattern in different regions since the mid-to-late-Holocene. Cloud formation processes may have a significant impact on precipitation, especially during the tropical marine processes and summer monsoon which convey abundant water vapor to coastal southern China and inland areas. Here, we use two 7500 year sedimentary records from the Pearl River Delta and the closed Maar Lake, respectively, in coastal southern China to reconstruct the mid-to-late-Holocene humidity variability and explore its possible relationship with cloud cover modulated by the Earth's magnetic fields (EMF). Our proxy records document an apparent increase in wetness in coastal southern China between 3.0 and 1.8 kyr BP. This apparent increase in humidity appears to be consistent with the lower virtual axial dipole moments and, in turn, with a lower EMF. This correlation suggests that the EMF might have been superimposed on the weakened monsoon to regulate the mid-to-late-Holocene hydroclimate in coastal southern China through the medium of galactic cosmic rays, aerosols, and cloud cover. However, further investigations are needed to verify this interaction.

Keywords hydroclimate variations, Earth's magnetic field, coastal southern China, the Holocene epoch

1 Introduction

Coastal southern China, which receives the oceanic moisture signal earlier when the Asian summer monsoon (ASM) blows inland toward China, has more complex hydroclimate patterns due to the superposition of the ASM and other low-latitude drivers. In particular, its hydrological conditions have differed significantly from the East Asian monsoonal precipitation variations since the Holocene. For example, the hydrologic conditions in coastal southern China showed a two-step increase in wetness during the middle to late Holocene (Yang et al., 2014), while most parts of the Chinese monsoon region showed a continuous decline in precipitation (Wang et al., 2005; Hu et al., 2008; Cai et al., 2010; Tan et al., 2018). The wet Little Ice Age in southern China is another major difference from the drier climate in central-northern China (e.g., Zhang et al., 2008; Yan et al., 2011; Zhang et al., 2018). These cases have led to the long-standing question of what drives the hydrological variability of coastal southern China to differ significantly from that of the East Asian monsoon region.

Recent studies have shown a significant positive correlation between aerosol, clouds, and precipitation (Pierce and Adams, 2007; Li et al., 2011; Campuzano et al., 2018; Jalihal et al., 2019; Liu et al., 2019). This is a fact that water vapor, whether carried by ASM or other drivers, inevitably forms clouds before falling to the ground as precipitation. Therefore, investigating the variation in cloud cover may help us more clearly to understand the mechanisms of hydroclimate change and the relationship between different driving forces. The process of cloud formation in the natural environment is affected by two factors, one is the content of water vapor and the other is the content of cloud condensation nuclei (CCN). The former is mainly transported by convection

Received December 20, 2021; accepted May 9, 2022

E-mail: eesyxq@mail.sysu.edu.cn

(e.g., ASM, ITCZ (intertropical convergence zone), ENSO (El Niño-Southern Oscillation)), while the latter is not only related to convection, but also contributes from some non-convective components. On the annual-decade scale, short-term wildfires and volcanic eruptions will release a large number of aerosol particles into the atmosphere (Robock and Outten, 2018; Jiang et al., 2020; Stenchikov, 2021). These aerosol particles increase the content of CCN in the atmosphere, which will increase precipitation after condensing with water vapor into raindrops. This also explains why heavy rainfall occurs after wildfires and volcanic eruptions. In addition, the variation of the non-convective CCN component may be related to the changes in the Earth's magnetic field (EMF). The EMF can indirectly influence the content of non-convective components in the CCN and cloud formation process by regulating the flux of galactic cosmic rays (GCRs) entering Earth's atmosphere (Dergachev et al., 2007; Kirkby, 2007; Knudsen and Riisager, 2009). Increased GCRs flux leads to increased atmosphere ionization and the nucleation rates of nanoscale particles, which can influence cloud formation when these nano-aerosols grow into CCN size (Carslaw et al., 2002; Kirkby et al., 2016; Svensmark et al., 2016; Svensmark et al., 2017; Cooper et al., 2021). However, the EMF modulation of climate on geological time scales has not been demonstrated and has long been debated due to the uncertainty of the forcing mechanism between them (Courtillot et al., 2007; Kirkby, 2007; Kerton, 2009; Knudsen and Riisager, 2009). Resolving Holocene hydroclimatic variations in coastal southern China will provide valid insights into the potential links among the EMF, cloud cover, and climate variation.

To explore potential links between low-latitude hydroclimate changes and the EMF during the Holocene, we constructed the mid-to-late-Holocene hydroclimate history. We did this at centennial-scale using the ratios of the relative content of hematite to the sum of hematite and goethite ($I_{Hm}/(I_{Hm} + I_{Gt})$ ratio) from the sediments deposited in the different environment. The formations of hematite and goethite in sediment are sensitive to hydrological variations and can reflect net precipitation (Long et al., 2011; Hyland et al., 2015; Zhang et al., 2020b). Therefore, the 7500 year $I_{Hm}/(I_{Hm} + I_{Gt})$ ratio profile in this study can fundamentally reveal the connections between EMF and hydroclimate at low latitudes.

2 Materials and methods

2.1 Materials and sampling

The Pearl River Delta stretches along the coastline of southern China between 21°40′ N and 23° N, and 112° E and 113°20′ E (Fig. 1(a)). It is shaped by the interactions between rivers and the South China Sea during the Late Quaternary. The West River and North River deltas occupy 93.4% of the area. From its catchment, the West River carries a large amount of sediment, mainly terrestrial detritus, into the South China Sea. Huguangyan Marr Lake, situated ~340 km to the south-west of the Pearl River Delta, is 2.3 km^2 in area, and ~20 m deep. It is surrounded by a high tephra wall with a shoal extending from north to south in the middle. With no natural inflows or outflows, its water balance is primarily controlled by precipitation and groundwater.

The Da Ao (DA) core (22°26.08′ N, 113°13.81′ E, total core length of 37.73 m, Fig. 1(b)) and Huguang Maar Lake (HML) core (21°9′ N, 110°17′ E, water depth of 11.5 m, total core length of 23 m, Fig. 1(c)) were obtained from the lower West River Delta and Huguangyan Maar Lake by using a modified Livingstone piston corer in 2015 A.D. and 2012 A.D., respectively. Two cores were retained inside PVC tubes and transported to the laboratory after drilling and preserved at a low temperature (~4°C) until sampling. The two cores were both split into halves, and one half from each core was continuously sampled by pushing cubic plastic boxes (2 cm× 2 cm× 2 cm) into the split surface for environmental magnetism analysis. Paired powder samples were also collected for additional analysis after the box samples were collected. A total of 880 and 786 samples were obtained from the DA and HML cores, respectively. Samples for diffuse reflectance spectroscopy analysis were collected at 5 cm and 7 cm intervals from the DA core (543 samples) and the HML core (110 samples of the upper 5 m), respectively.

Dating samples of multiple materials (e.g., tree branches, leaves, plant fragments) were collected from the two cores and sent to three laboratories for accelerator mass spectrometry (AMS) radiocarbon dating. We also collected seven optically stimulated luminescence (OSL) samples and sent them to Qinghai Institute of Salt Lakes, Chinese Academy of Sciences, for OSL dating.

2.2 Experimental methods

Diffuse reflectance spectroscopy (DRS) was used to obtain the relative concentration of hematite (I_{Hm}) and goethite (I_{Gt}) and the $I_{Hm}/(I_{Hm} + I_{Gt})$ ratio. The DRS was conducted at the Geophysical Laboratory, Sun Yat-sen University, conducted on a PerkinElmer Lambda 950 spectrophotometer with a diffuse reflectance attachment (reflectance sphere) following the analytical protocols described in Zhang et al. (2020b). The data processing procedure followed Torrent and Barrón (2008) and Scheinost (1998).

Cubic samples (2 cm× 2 cm× 2 cm) were analyzed for the low-field magnetic volume susceptibility (κ) by using a Kappabridge MFK1-FA with a frequency of 976 Hz. A total of 880 and 230 were measured for the DA core and the upper 5 m of the HML core, respectively. Natural

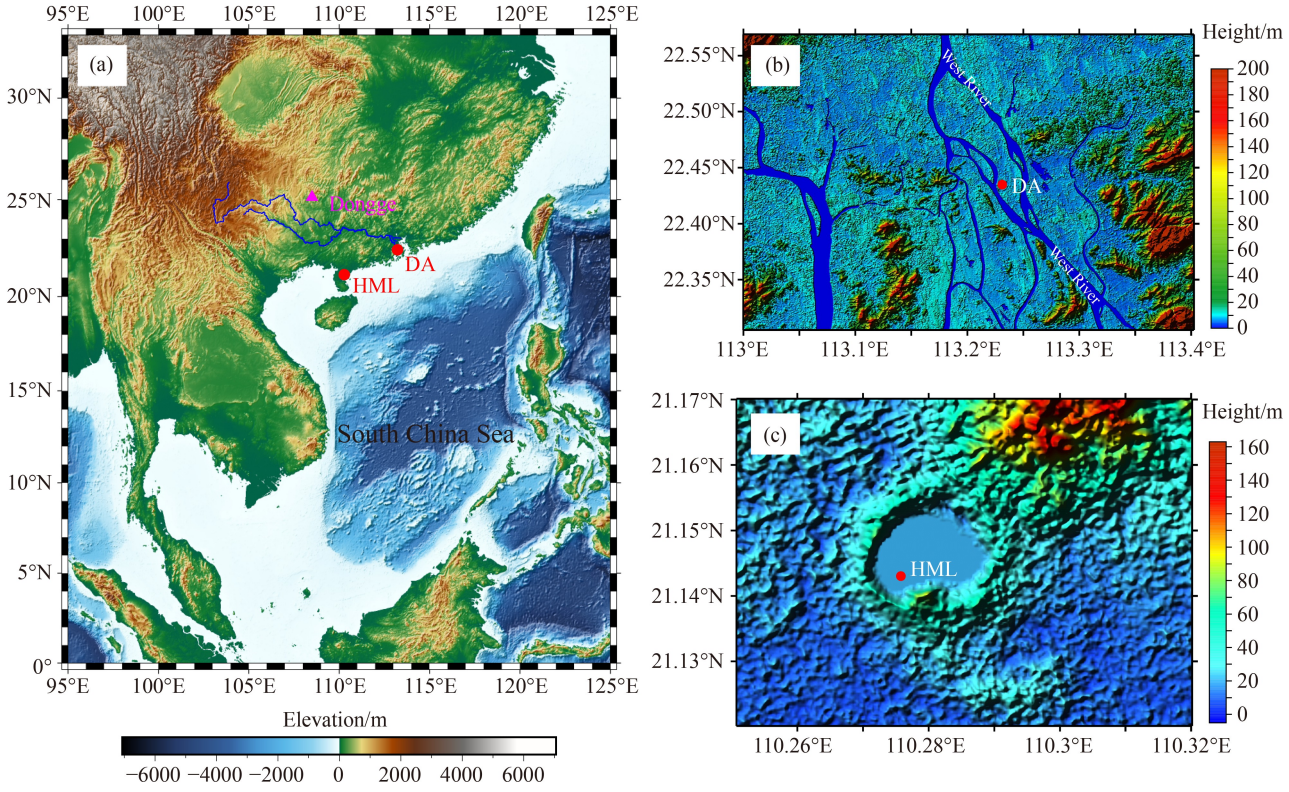

Fig. 1 (a) Geographical locations of the DA and HML sites (red circles) and the other sites mentioned in the paper (purple triangles). The Pearl River is shown (in blue line). (b) and (c) are enlarged maps of the locations of the DA and HML cores, respectively.

remanent magnetization (NRM) was stepwise demagnetized with 2G-760 system using peak fields of 0–80 mT (total of 12 steps). Anhysteretic remanence (ARM) was then imparted with a 0.05 mT steady field and an 80 mT alternating field. ARM was demagnetized and measured in 40 mT field. Isothermal remanence was imposed using a DC field of 1 T (SIRM) and 100 mT (IRM_{-100mT}). ARM and IRM were measured using JR6A Spinner Magnetometer. ARM and IRM were measured for all cubic subsamples of the DA core. Representative samples of the DA core (n = 4) were selected to perform rock magnetism analysis. Temperature-independent susceptibility (χ-T) curves were measured using the same Kappabridge magnetometer from room temperature to 700°C in an argon environment. The hysteresis loops and first-order reversal curves (FORCs) were measured using a Princeton Measurements Corporation vibrating sample magnetometer (MircoMag 3900). Hysteresis loops were obtained between −1 to 1 T with a field increment of 10 mT. The saturation magnetization (M_s), saturation remanence (M_{rs}), and coercivity (B_c) were obtained from the hysteresis loops. The coercivity of the remanence (B_{cr}) was determined using the demagnetized curve of M_{rs}. FORC measurements were conducted by 150 hysteresis loop curves with a 1 s averaging time and a field step of 2 mT and then processed with the FORCinel software v3.06 (Harrison and Feinberg, 2008). Natural remanent magnetization was performed at the Paleomagnetism and Geochronology Laboratory, Institute of Geology and Geophysics, Chinese Academy of Sciences, China. The other rock magnetism measurements were conducted at the Geophysical Laboratory, Sun Yat-sen University.

The bulk organic matter ($\delta^{13}C$) was also measured for the upper 27.3 m of the DA core (232 samples). After treatment with 5% HCl to remove carbonates, the bulk organic matter $\delta^{13}C$ value was measured using a Finnigan MAT Delta Plus mass spectrometer coupled with a Flash EA 1112 elemental analyzer at State Key Laboratory of Organic Geochemistry, Guangzhou Institute of Geochemistry, Chinese Academy of Sciences, China. The isotopic values are presented in the standard δ-notation in per mil (‰) deviation from the Pee Dee Belemnite (PDB). Replicate analyses indicated that the analytical precision was better than 0.1‰.

2.3 Meteorological data and analytical methods

A variety of meteorological data are used in this paper. Monthly long-term mean temperature (CMA_{tmp}) and precipitation (CMA_{pre}) data (1981–2010) of Zhanjiang and Xinhui meteorological stations were obtained from the CMA Meteorological Data Centre (available at CMA website). The monthly long-term mean wind data

(1981–2010) were obtained from the NCEP/DOE Reanalysis II data set with a 2.5-degree spatial resolution and 17 vertical levels (Kanamitsu et al., 2002). The long-term mean of monthly total precipitation ($GPCC_{pre}$) data (1981–2010) were obtained from the Global Precipitation Climatology Centre (GPCC) monthly precipitation data set (V2018) with a 0.5-degree spatial resolution (Schneider et al., 2018). The global monthly mean precipitation (CRU_{pre}), self-calibrating Palmer drought severity index (CRU_{scPDSI}), and cloud (CRU_{cld}) data (1901–2010) were obtained from CRU TS V4.03 climatic data sets, which have a 0.5-degree spatial resolution (Harris et al., 2020).

Air-mass back-trajectory analyses of the HML and DA cores in summer (June–July–August) were performed using the HYSPLIT V4.8 model and based on the NCEP/NCAR Reanalysis data set from 2009 to 2019 (Kalnay et al., 1996). The back trajectories were computed for a time period of 96 h (sampled four times per day at 00 UTC, 06 UTC, 12 UTC, and 18 UTC) and started at 1500 m above ground level. Similar trajectories were merged through cluster analysis.

3 Results

3.1 Modern climatology

The instrumental data show that the lower reaches of the Pearl River Delta and Huguangyan Marr Lake have a typical monsoonal climate, and approximately 75% of the annual precipitation is supplied between May and September (Figs. 2(a) and 2(b)). Modern precipitation is mainly influenced by the East Asian summer monsoon (EASM) and the Indian summer monsoon (ISM; Fig. 2(c)). The ocean-atmospheric circulations such as the Hadley circulation and the Walker circulation also have a significant influence on the region (Zhang et al., 2020a). The Air-mass back-trajectory analysis results for the HML and DA cores show that the water vapor of coastal southern China in summer is mainly transported from the South China Sea, the Indian Ocean, and the Western Pacific area by the EASM and the ISM (Fig. 2(c)). The profiles of vertical velocity and meridional wind at 112.5°E show that there is an updraft over coastal southern China in summer due to the increased temperature of land (Figs. 2(d) and 2(e)). This updraft will impede most of the water vapor which is carried by ASM and other forcing, and force the remaining water vapor to rise higher and then migrate to inland regions. Therefore, the total precipitation in coastal southern China is higher than that in inland areas (Fig. 2(c)). The pointwise correlation results between cloud cover and precipitation and scPDSI show that clouds play a non-negligible role in regulating precipitation in the monsoon region (Figs. 2(f) and 2(g)). The following connection can explain the relationship between cloud cover and precipitation: water vapor combines with cloud condensation nuclei (CCN) to form raindrops → large numbers of raindrops gather together and form clouds → raindrops fall to ground when the raindrops grow large (heavy) enough such that the clouds cannot carry them. Therefore, when there are more clouds, precipitation increases, and vice versa.

3.2 Chronology

The AMS dating results of the two cores are shown in Table 1. All of the dates were calibrated using the IntCal 13 data set in the CALIB 7.04 program (Stuiver et al., 2020). In the DA core, six of seven OSL ages are in good agreement with the AMS ^{14}C ages (Table S1), which further demonstrates the reliability and accuracy of the AMS ^{14}C dating. The OSL ages were not considered when reconstructing the age-depth model. We assumed that −65 yrs. BP (2015 A.D.) and −62 yrs. BP (2012 A.D.) are the ages of the tops of DA and HML cores, respectively. The detailed age controls for cores DA and HML are based on a series of 14 AMS ^{14}C ages and 4 AMS ^{14}C ages, respectively. The age-depth models of two cores were developed using a Bayesian approach with the Bacon program (Blaauw and Christen, 2011). The age models show continuous sedimentation records without hiatuses in two cores, reaching back to 7.5 kyr BP and 8 kyr BP for the DA core and the upper 5 m of the HML core, respectively (Fig. 3).

Age offsets arising from the radiocarbon reservoir effect in the different deposition environment is negligible to the chronology of two cores. In HML, the good agreement of AMS ages from multiple materials at the same depth is observed (the deviation is less than 100 years), indicating a negligible reservoir effect in this freshwater lake (Wu et al., 2012). In Pearl River Delta regions, a relatively low marine reservoir effect (ΔR = −128 ± 40 years) is reported based on the average radiocarbon age of modern corals from Hong Kong, which indicate that the source waters entering the South China Sea are rather well equilibrated with atmospheric ^{14}C (Southon et al., 2002). Therefore, the radiocarbon reservoir effect is minor and ignorable in two cores and does not affect the variation of climate proxies we discussed later at the centennial-scale.

3.3 Downcore variations of environmental proxies

Downcore variations of the κ, $\delta^{13}C$, I_{Hm}, I_{Gt}, and the $I_{Hm}/(I_{Hm} + I_{Gt})$ ratio of two cores are shown in Fig. 4. The magnetic susceptibility of two cores was characterized by a two-stage change: a low value stage and a high value stage. The $\delta^{13}C_{TOC}$ record from the HML lake (Liu et al., 2019) and $\delta^{13}C$ record from the DA core show a consistent trend during the overlapping time interval. The

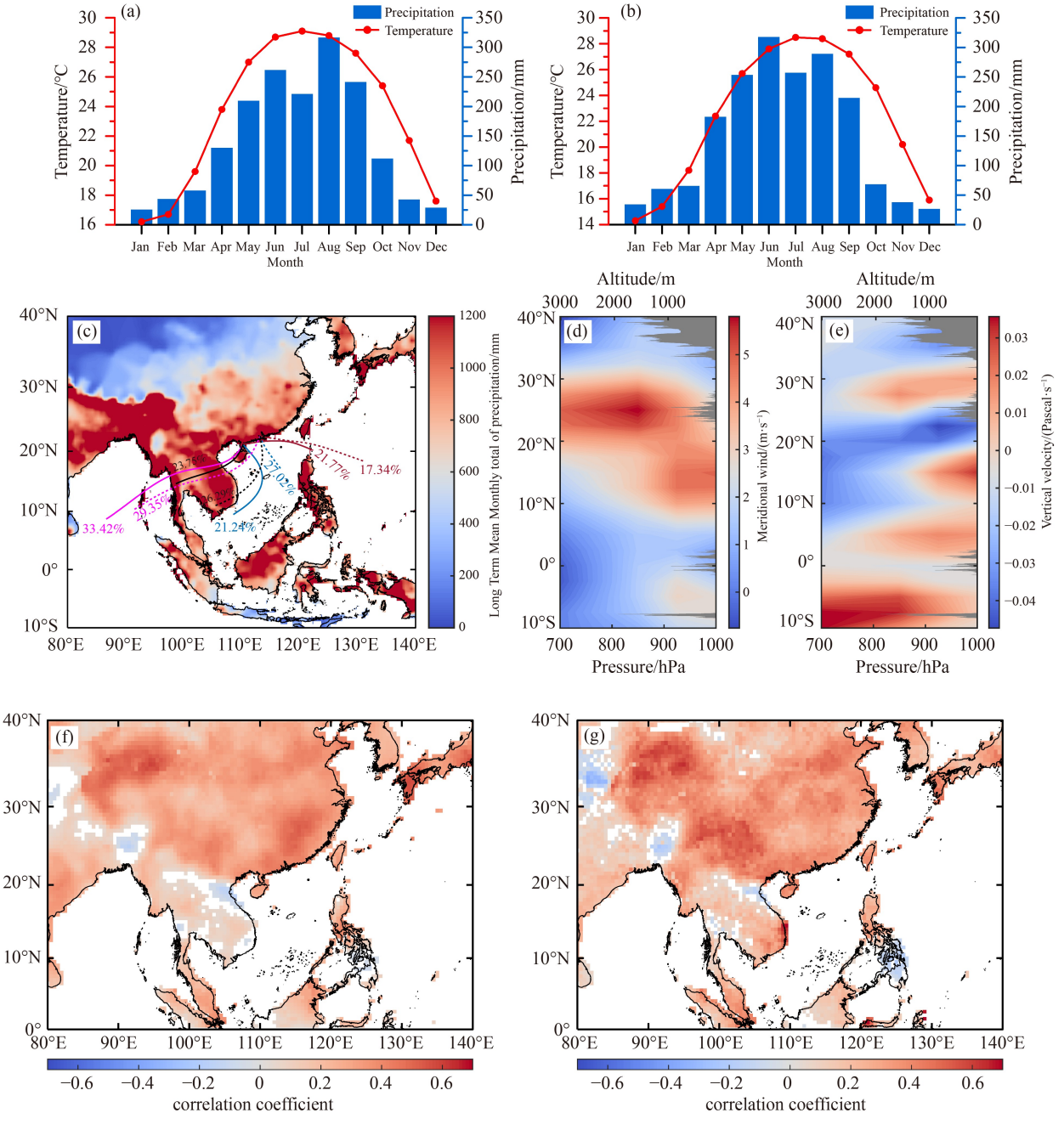

Fig. 2 Modern climatology of the study sites. (a–b) Long-term mean monthly temperature (CMA_{tmp}) and precipitation (CMA_{pre}) distributions at the Zhanjiang meteorology station (~1.73 km from the HML core) and Xinhui meteorology station (~19.67 km from the DA core) between 1981 and 2010, respectively. (c) Long-term means monthly total precipitation ($GPCC_{pre}$) in MJJAS (May to September) during 1981–2010. The results of the air mass back trajectories analysis of the HML core (solid line) and DA core (dashed line) are also shown. (d–e) Vertical profile of zonal wind and vertical velocity at 112.5°E from 10°S to 40°N, respectively. The gray shading represents the terrain. (f–g) Spatial correlations ($p < 0.01$) of cloud cover (CRU_{cld}) with monthly precipitation (CRU_{pre}) and scPDSI (CRU_{scPDSI}) from 1901 to 2010, respectively.

relative hematite (I_{Hm}) and goethite (I_{Gt}) concentrations in two cores showed an increasing trend over the past 7.5 kyr BP (Fig. 4), and a substantial increase was particularly displayed since ~2 kyr BP. The $I_{Hm}/(I_{Hm} + I_{Gt})$ profiles of the two cores also show consistent variations at the centennial-scale, which is supported by the results of the correlation analysis between the first principal component of two cores (Fig. S1). The high value of magnetic susceptibility and the good positive correlation of $I_{Hm}/(I_{Hm} + I_{Gt})$ records in two cores during the past 2 kyr indicate that the influence of human activities on the amount of terrestrial input and the ratio of magnetic minerals in the sediments is negligible compared to natural processes.

Table 1 AMS radiocarbon dates from the HML and DA cores

Sample ID	Depth/m	Material	^{14}C age/ (yrs. BP*)	Error/ (± yrs.)	Calibrated age/ (cal. yrs. BP, 2σ)	Mean age/ (cal. yrs. BP)
HML-1-1-29[a)]	0.64	Tree branches	175	30	135–225	180
HML-2-1-35[a)]	2.52	Twig	2530	25	2497–2595	2546
HML-2-2-9[a)]	3.27	Leaves	3475	30	3685–3834	3759.5
HML-2-2-71[a)]	4.57	Plant fragments	5540	35	6288–6399	6343.5
DA3-C-2[a)]	6.09	Plant fragments	185	20	143–217	180
DA4-C-3[a)]	7.06	Plant fragments	235	20	281–307	294
DA4-C-1[b)]	7.34	Plant fragments	350	30	310–500	405
DA7-C-1[a)]	11.89	Plant fragments	1370	20	1275–1311	1293
DA8-C-1[a)]	14.28	Plant fragments	1745	30	1566–1718	1642
DA11-C-1[b)]	19.76	Conch	1990	30	1880–1995	1937.5
DA16-C-1[b)]	27.19	Conch	3400	30	3576–3700	3638
DA17-C-1[c)]	29.15	Conch	4225	25	4809–4851	4830
DA18-C-1[c)]	31.12	Shell	4500	25	5047–5201	5124
DA19-C-1[c)]	31.83	Shell	4505	25	5048–5196	5122
DA20-C-2 [c)]	34.61	Shell	5455	25	6260–6299	6279.5
DA21-C-1[c)]	35.33	Shell	5660	25	6400–6494	6447
DA22-C-2[c)]	36.94	Shell	6390	25	7266–7338	7302
DA23-C-3[c)]	37.26	Shell	6530	25	7420–7485	7452.5

a) Peking University AMS Laboratory. b) Beta Analytic Inc., Florida (USA). c) State Key Laboratory of Organic Geochemistry, Guangzhou Institute of Geochemistry, Chinese Academy of Sciences. *. BP: before 1950 A.D.

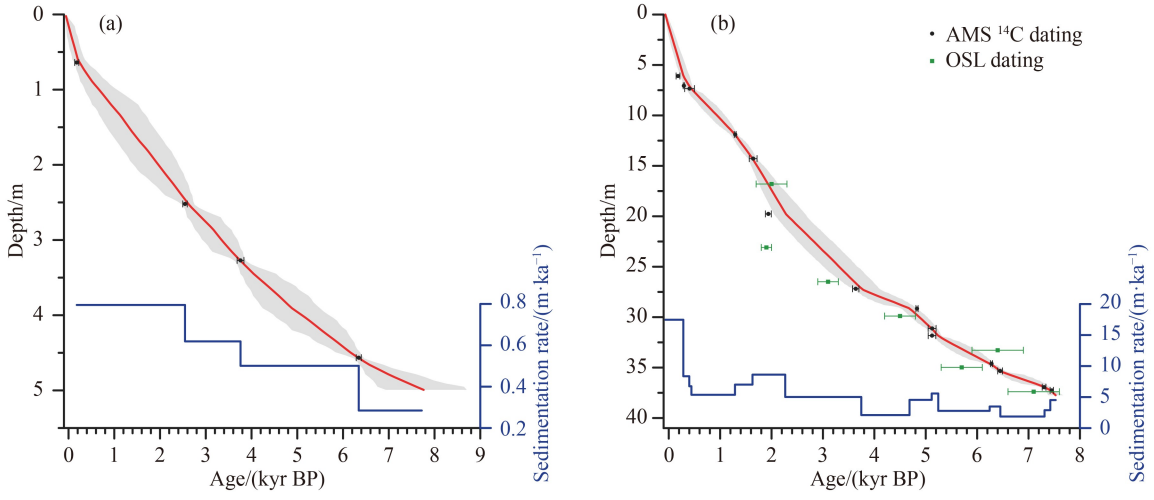

Fig. 3 Age models and sedimentation rates for the (a) HML core and (b) DA core. The age models were computed using the Bacon software (Blaauw and Christen, 2011). Seven OSL ages (green rectangles with error bars) in (b) were not taken into account to construct the age-model of DA core. The red lines represent the fitted weighted-mean ages, and the shaded areas indicate 2-sigma uncertainties.

4 Discussion

4.1 The paleoclimate significance of the ratio of hematite and goethite contents

The formation of hematite and goethite in soil and sediments varies with climate (Schwertmann, 1988). The formation of goethite and hematite is closely related to hydroclimate, with warm, dry climates favoring hematite formation and wet, cold climates favoring goethite formation (Schwertmann, 1988; Ji et al., 2004; Zhang et al., 2007). Therefore, ratios related to their concentration, such as Hm/Gt and $I_{Hm}/(I_{Hm} + I_{Gt})$, are often used as indices of hydrological variations (e.g., Ji et al., 2004;

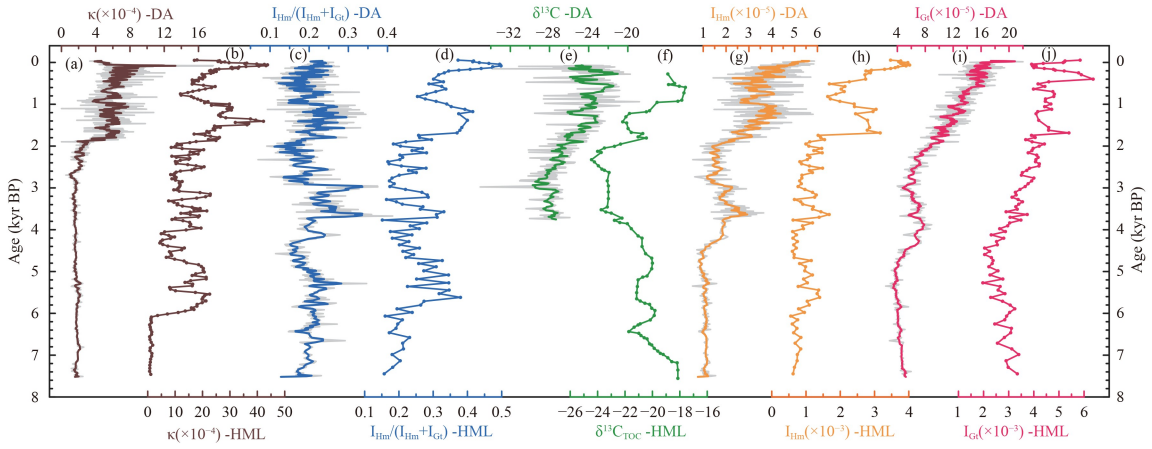

Fig. 4 Downcores variations in environmental proxies from the DA and HML cores. (a–b) Magnetic susceptibility (κ); (c–d) $I_{Hm}/(I_{Hm} + I_{Gt})$; (e) $\delta^{13}C$; (f) $\delta^{13}C_{TOC}$ in HML (Liu et al., 2005); (g–h) I_{Hm}; and (i–j) I_{Gt}. The gray lines in (a), (c), (e), (g), and (i) are the raw data of records in core DA, and the 3-point moving average smoothed values are displayed by the colored lines.

Zhang et al., 2020b). However, the dissolution of magnetic minerals in a reducing environment needs to be considered for lake sediment (Robinson et al., 2000; Abrajevitch and Kodama, 2011; Duan et al., 2014). There was a reduction environment in the HML record before 6.0 kyr BP and dissolution is partially responsible for the phenomenon of weak magnetism with coarser grain size (Duan et al., 2014). The magnetic susceptibility of the DA core is lower before ~2 kyr BP (Fig. 4 and Fig. S2), indicating lower concentrations of magnetic minerals. Nevertheless, the rock magnetic results of representative samples show that the magnetic minerals in the lower κ layers have finer grain sizes than those in the higher κ layers, inconsistent with the notion that dissolution leads to weak magnetism (Fig. S2). In addition, the magnetic minerals in the DA core are dominated by low-coercivity minerals (Fig. S3). The dissolution effect of magnetic minerals cannot be ruled out; however, this process may have a relatively minor impact, and the lower κ value during the interval before 2.0 kyr BP could mainly result from a decreased terrigenous material flux. In addition, HML $I_{Hm}/(I_{Hm} + I_{Gt})$ profile shows high consistency with its $\delta^{13}C_{TOC}$ record, which is controlled by effective precipitation and finally by EASM and ISM (Liu et al., 2005; Fig. 2). The $\delta^{13}C$ and $I_{Hm}/(I_{Hm} + I_{Gt})$ trends in the DA core are also generally consistent over the past 4.0 kyr (Fig. 2). The $I_{Hm}/(I_{Hm} + I_{Gt})$ record from the DA core is highly consistent with the Palmer drought severity index (PDSI) records, which represent the precipitation in south-eastern China during the period of 1620–2000 A.D. (Liu et al., 2019; Fig. 5). The $I_{Hm}/(I_{Hm} + I_{Gt})$ trends of the two cores show a good comparison at the centennial scale (Fig. S1). These results suggest that the $I_{Hm}/(I_{Hm} + I_{Gt})$ ratios in the HML and DA cores can be indicative of effective rainfall in coastal southern China. The decreased (increased) precipitation is beneficial for the environment of hematite (goethite) formation, and the corresponding decreasing (increasing) terrigenous flux. Ultimately, this climate process would induce the high (low) $I_{Hm}/(I_{Hm} + I_{Gt})$ ratios.

4.2 Hydroclimate variations in coastal southern China and changes in Earth's magnetic field

The most profound feature of our $I_{Hm}/(I_{Hm} + I_{Gt})$ records is that a significant decline from 3.0 to 1.8 kyr BP

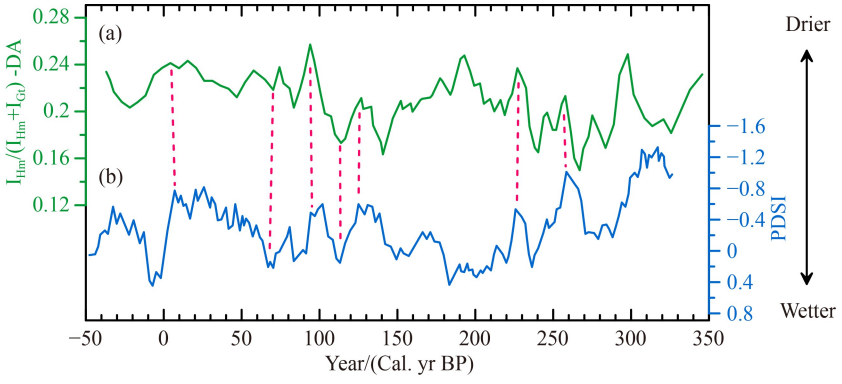

Fig. 5 Comparison of the $I_{Hm}/(I_{Hm} + I_{Gt})$ record from the DA core and the PDSI record from Mt. Tianmu, which is located in the southern lower reaches of the Yangtze River (Liu et al., 2019).

superimposed on the long-term increasing trend over the past 7.5 kyr BP (Figs. 6(b) and 6(c)). This signifies extreme wetness in coastal southern China over 3.0−1.8 kyr BP, approaching or even exceeding that of the mid-Holocene, which is notably inconsistent with the continuous weakening trend of ASM and Northern Hemisphere summer insolation (Wang et al., 2005; Laskar et al., 2011; Kathayat et al., 2016; Wang et al., 2016; Zhang et al., 2017; Xu et al., 2020). In addition, this centennial-scale increase in rainfall is also recognizable in the paleontology records of HML (Zhang et al., 2020a), peat records, and stalagmite records in central China (Xie et al., 2013; Zhu et al., 2017; Zhang et al., 2021). The different trends among different regions may be related to the complex precipitation patterns in East Asia (Hao et al., 2016). Moreover, previous studies demonstrated that the ocean-atmosphere variabilities, such as a southward migration of the ITCZ, strong ENSO activity, south-westward shift of WPSH, accounted for the late Holocene humidity of coastal southern China during the long-term weakened Asian monsoon trend (Yang et al., 2012; Yang et al., 2014; Xu et al., 2020; Zhang et al., 2020a). However, ITCZ displacement and ENSO activity are difficult to fully reconcile with the humidity conditions over 3.0−1.8 ka BP inferred from our records (Haug et al., 2001; Conroy et al., 2008; Fig. S4). All of these results suggest that the humidity over 3.0−1.8 kyr BP inferred from our $I_{Hm}/(I_{Hm} + I_{Gt})$ records is

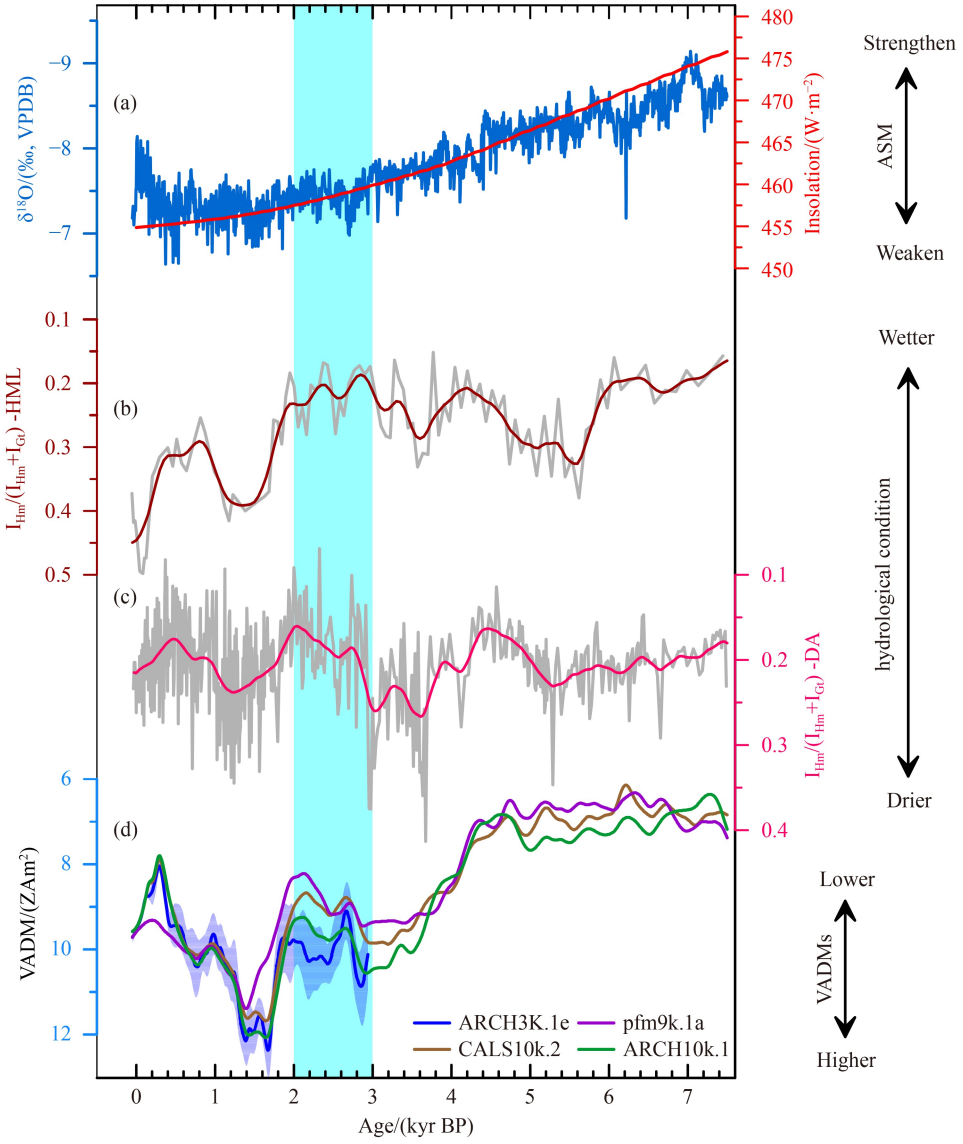

Fig. 6 Comparison of $I_{Hm}/(I_{Hm} + I_{Gt})$ records from the HML and DA cores with the Asian monsoon, summer insolation, and the virtual dipole moment records. (a) The stalagmite $\delta^{18}O$ record from Dongge Cave (navy blue, Wang et al., 2005) and summer insolation at 22°N (red, Laskar et al., 2011). (b and c) The $I_{Hm}/(I_{Hm} + I_{Gt})$ records from the HML and DA cores in this study, respectively. (d) Predictions of the virtual dipole moment records in East Asia from global models (Korte et al., 2009; Nilsson et al., 2014; Constable et al., 2016). The blue bar indicates humid conditions during 3.0−1.8 kyr BP corresponding to lower VADMs.

unlikely to be ascribed to AM-coupled hydroclimate variations.

The general trend of our $I_{Hm}/(I_{Hm} + I_{Gt})$ records is highly similar to that of the virtual axial dipole moments (VADMs) from multiple global models, with higher $I_{Hm}/(I_{Hm} + I_{Gt})$ ratios corresponding to strong VADMs, and vice versa (Fig. 6). This high similarity has been particularly evident over the past 3 kyr BP. It appears that greater precipitation in coastal southern China is associated with a lower Earth's magnetic field and less precipitation with a higher Earth's magnetic field. Further, a strong positive correlation was detected between the EMF records in southern China and our records from DA (r = 0.7503, p < 0.01; Fig. S5) and HML (r = 0.6893, p < 0.01; Fig. S5) during the past 3 kyr. This puts the hydrologic variations in coastal southern China over 3.0–1.8 ka BP to a possible connection with the EMF-GCRs-Aerosols-Cloud-Climate. The link between EMF and climate is complex and has been debated for decades. Researchers found that ozone and aerosol play an important role in climate change and their fluctuating are inextricably linked to the EMF variations (Carslaw et al., 2002; Kirkby, 2007; Channell and Vigliotti, 2019; Cooper et al., 2021). Based on the EMF-GCRs-climate interaction in Cooper et al. (2021) and Kirkby (2007), the EMF regulates the flux of GCRs particles entering Earth's atmosphere, which then influences ionization in the troposphere, and then influences the production of new aerosol particles and the concentration of ozone in the atmosphere, which affects the formation of clouds and ultimately influences climate (Gallet et al., 2005; Dergachev et al., 2007; Kirkby, 2007; Kerton, 2009; Knudsen and Riisager, 2009; Cooper et al., 2021). The positive correlation between cloud cover and precipitation has been detected from modern observations (Fig. 2). Notably, water vapor and CCN are two necessary conditions required for cloud formation. The increased CCN will reduce the threshold of the condensation reaction and result in more vapor condensing into droplets (Li et al., 2011; Sato et al., 2018; Williamson et al., 2019; Luo et al., 2021). In contrast, if too few CCNs (water vapor) are present, precipitation will not increase even if more water vapor (CCNs) is available (Li et al., 2011). As we mentioned above, the water vapor is abundant in coastal southern China, and a small increase in CCN may lead to significantly increased precipitation, and vice versa. During the weak EMF intervals, the weak shielding allows more GCRs to enter the Earth's troposphere, and then produces an increasing number of small ions (charged molecules or small charged clusters of molecules) in the troposphere, which increases the nucleation rates of nanoscale aerosol particles and finally influences the formation process of clouds (Pierce and Adams, 2007; Svensmark et al., 2016; Pierce, 2017; Campuzano et al., 2018; Cooper et al., 2021). More importantly, weak EMF shielding also reduces the energy threshold for the particles to reach the lower latitude regions, increasing the concentration of ion and aerosol nucleation and CCN in the lower latitude atmosphere (Fig. 7). Correspondingly, precipitation increased in coastal southern China. During the strong EMF intervals, fewer GCRs are allowed to enter the Earth's troposphere and most of them can only cause nuclear reactions at the high geomagnetic latitudes. In the lower latitude regions, the climate effect by the GCRs modulated nanoscale aerosol particles is not expected to be more significant than weak EMF intervals. Moreover, the increased EMF is superimposed on the weakening summer insolation and ASM (e.g., 4.0–3.0 kyr BP and 1.8–1.4 kyr BP in Fig. 6), which lead to decreased precipitation and drier hydroclimate conditions.

It is important to note that the forcing mechanisms of climate change are more complex than we mentioned above. The correlation between the $I_{Hm}/(I_{Hm} + I_{Gt})$

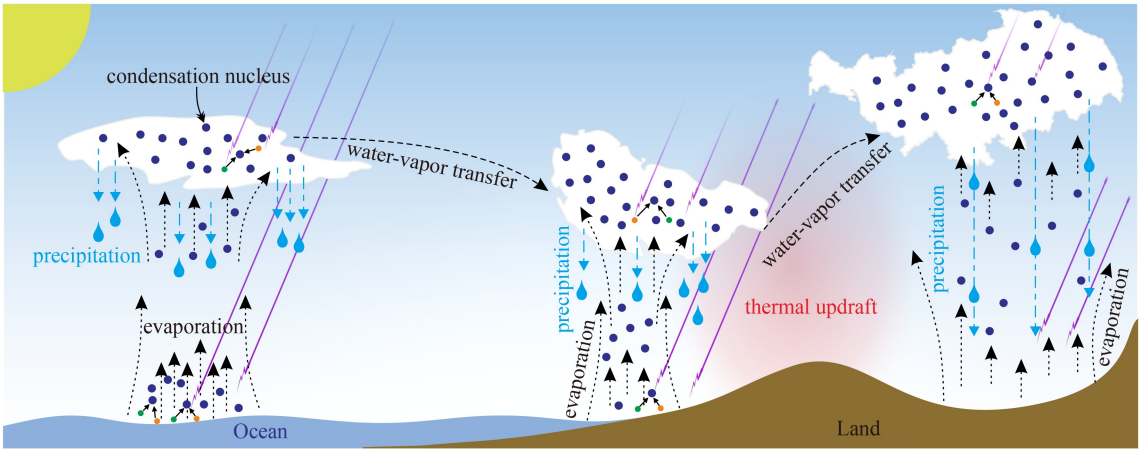

Fig. 7 Schematic diagram demonstrating the hydroclimate variability during low-EMF periods. With a decrease in EMF intensity, a high density of GCRs leads to an increase in condensation nuclei, which results in a wetter hydrological condition. Solar radiation, total water vapor, and evaporation are assumed to be constant in this diagram.

records and EMF variations does not imply that the EMF and cloud cover are the dominant force driving hydroclimate change in low-latitude regions. This is a superimposed result of multiple forcing mechanisms, such as ASM, ITCZ, ENSO, WPSH, human activities, and EMF-GCR-Aerosols-Clouds-Climate interactions.

5 Conclusions

We provide high-resolution $I_{Hm}/(I_{Hm} + I_{Gt})$ records revealing hydroclimate variations in coastal southern China during the mid-to-late-Holocene. The region experienced profound humidity during 3.0–1.8 kyr BP, which differs from the East Asian monsoon variability. The correlations between our $I_{Hm}/(I_{Hm} + I_{Gt})$ records and the virtual axial dipole moments, suggest that the Earth's magnetic field played an indispensable role in regulating the mid-to-late-Holocene hydroclimate in coastal southern China, with the GCRs and aerosols and cloud cover as the medium. The Earth's magnetic field may act in combination with other mechanisms. Although this work appears to provide support for the connection between the EMF and climate, future investigations are needed to further discuss this issue.

Acknowledgments This research is supported by the projects of National Second Expedition to the Tibetan Plateau (No. 2019QZKK0707), Guangdong Province Introduced Innovative R&D Team of Geological Processes and Natural Disasters around the South China Sea (No. 2016ZT06N331), the projects of National Natural Science Foundation of China (Grant Nos. 41872217, 41672162, and 41904068) and the Natural Science Foundation of Guangdong Province (No. 2018B030311064).

Supplementary material is available in the online version of this article at https://doi.org/10.1007/s11707-022-1009-y and is accessible for authorized users.

Competing interests The authors declare that they have no competing interests.

References

Abrajevitch A, Kodama K (2011). Diagenetic sensitivity of paleoenvironmental proxies: a rock magnetic study of Australian continental margin sediments. Geochem Geophys Geosyst, 12(5): Q05Z24

Blaauw M, Christen J (2011). Flexible paleoclimate age-depth models using an autoregressive gamma process. Bayesian Anal, 6(3): 457–474

Cai Y, Tan L, Cheng H, An Z, Edwards R L, Kelly M J, Kong X, Wang X (2010). The variation of summer monsoon precipitation in central China since the last deglaciation. Earth Planet Sci Lett, 291(1–4): 21–31

Campuzano S A, De Santis A, Pavón-Carrasco F J, Osete M L, Qamili E (2018). New perspectives in the study of the Earth's magnetic field and climate connection: the use of transfer entropy. PLoS One, 13(11): e0207270

Carslaw K S, Harrison R G, Kirkby J (2002). Cosmic rays, clouds, and climate. Science, 298(5599): 1732–1737

Channell J E T, Vigliotti L (2019). The role of geomagnetic field intensity in Late Quaternary evolution of humans and large mammals. Rev Geophys, 57(3): 709–738

Constable C, Korte M, Panovska S (2016). Persistent high paleosecular variation activity in southern hemisphere for at least 10000 years. Earth Planet Sci Lett, 453: 78–86

Conroy J L, Overpeck J T, Cole J E, Shanahan T M, Steinitz-Kannan M (2008). Holocene changes in eastern tropical Pacific climate inferred from a Galápagos lake sediment record. Quat Sci Rev, 27(11–12): 1166–1180

Cooper A, Turney C S M, Palmer J, Hogg A, McGlone M, Wilmshurst J, Lorrey A M, Heaton T J, Russell J M, McCracken K, Anet J G, Rozanov E, Friedel M, Suter I, Peter T, Muscheler R, Adolphi F, Dosseto A, Faith J T, Fenwick P, Fogwill C J, Hughen K, Lipson M, Liu J, Nowaczyk N, Rainsley E, Bronk Ramsey C, Sebastianelli P, Souilmi Y, Stevenson J, Thomas Z, Tobler R, Zech R (2021). A global environmental crisis 42000 years ago. Science, 371(6531): 811–818

Courtillot V, Gallet Y, Le Mouël J L, Fluteau F, Genevey A (2007). Are there connections between the Earth's magnetic field and climate? Earth Planet Sci Lett, 253(3–4): 328–339

Dergachev V A, Dmitriev P B, Raspopov O M, Jungner H (2007). Cosmic ray flux variations, modulated by the solar and terrestrial magnetic fields, and climate changes. Part 2: the time interval from ~10000 to ~100000 years ago. Geomagn Aeron, 47(1): 109–117

Duan Z, Liu Q, Yang X, Gao X, Su Y (2014). Magnetism of the Huguangyan Maar Lake sediments, Southeast China and its paleoenvironmental implications. Palaeogeogr Palaeoclimatol Palaeoecol, 395: 158–167

Gallet Y, Genevey A, Fluteau F (2005). Does Earth's magnetic field secular variation control centennial climate change? Earth Planet Sci Lett, 236(1–2): 339–347

Hao Z, Zheng J, Zhang X, Liu H, Li M, Ge Q (2016). Spatial patterns of precipitation anomalies in eastern China during centennial cold and warm periods of the past 2000 years. Int J Climatol, 36(1): 467–475

Harris I, Osborn T J, Jones P, Lister D (2020). Version 4 of the CRU TS monthly high-resolution gridded multivariate climate dataset. Sci Data, 7(1): 109

Harrison R J, Feinberg J M (2008). FORCinel: an improved algorithm for calculating first-order reversal curve distributions using locally weighted regression smoothing. Geochem Geophys Geosyst, 9(5): Q05016

Haug G H, Hughen K A, Sigman D M, Peterson L C, Röhl U (2001). Southward migration of the intertropical convergence zone through the Holocene. Science, 293(5533): 1304–1308

Hu C, Henderson G M, Huang J, Xie S, Sun Y, Johnson K R (2008). Quantification of Holocene Asian monsoon rainfall from spatially separated cave records. Earth Planet Sci Lett, 266(3–4): 221–232

Hyland E G, Sheldon N D, Van der Voo R, Badgley C, Abrajevitch A (2015). A new paleoprecipitation proxy based on soil magnetic properties: implications for expanding paleoclimate reconstructions.

Geol Soc Am Bull, 127(7–8): 975–981

Jalihal C, Srinivasan J, Chakraborty A (2019). Modulation of Indian monsoon by water vapor and cloud feedback over the past 22,000 years. Nat Commun, 10(1): 5701

Ji J F, Chen J, Balsam W, Lu H Y, Sun Y B, Xu H F (2004). High resolution hematite/goethite records from Chinese loess sequences for the last glacial-interglacial cycle: rapid climatic response of the East Asian Monsoon to the tropical Pacific. Geophys Res Lett, 31(3): L03207

Jiang Y, Yang X Q, Liu X, Qian Y, Zhang K, Wang M, Li F, Wang Y, Lu Z (2020). Impacts of wildfire aerosols on global energy budget and climate: the role of climate feedbacks. J Clim, 33(8): 3351–3366

Kalnay E, Kanamitsu M, Kistler R, Collins W, Deaven D, Gandin L, Iredell M, Saha S, White G, Woollen J, Zhu Y, Leetmaa A, Reynolds R, Chelliah M, Ebisuzaki W, Higgins W, Janowiak J, Mo K C, Ropelewski C, Wang J, Jenne R, Joseph D (1996). The NCEP/NCAR 40-year reanalysis project. Bull Am Meteorol Soc, 77(3): 437–472

Kanamitsu M, Ebisuzaki W, Woollen J, Yang S K, Hnilo J J, Fiorino M, Potter G L (2002). NCEP–DOE AMIP-II reanalysis (R-2). Bull Am Meteorol Soc, 83(11): 1631–1644

Kathayat G, Cheng H, Sinha A, Spötl C, Edwards R L, Zhang H, Li X, Yi L, Ning Y, Cai Y, Lui W L, Breitenbach S F (2016). Indian monsoon variability on millennial-orbital timescales. Sci Rep, 6(1): 24374

Kerton A K (2009). Climate change and the Earth's magnetic poles, a possible connection. Energy Environ, 20(1): 75–83

Kirkby J (2007). Cosmic rays and climate. Surv Geophys, 28(5–6): 333–375

Kirkby J, Duplissy J, Sengupta K, Frege C, Gordon H, Williamson C, Heinritzi M, Simon M, Yan C, Almeida J, Tröstl J, Nieminen T, Ortega I K, Wagner R, Adamov A, Amorim A, Bernhammer A K, Bianchi F, Breitenlechner M, Brilke S, Chen X, Craven J, Dias A, Ehrhart S, Flagan R C, Franchin A, Fuchs C, Guida R, Hakala J, Hoyle C R, Jokinen T, Junninen H, Kangasluoma J, Kim J, Krapf M, Kürten A, Laaksonen A, Lehtipalo K, Makhmutov V, Mathot S, Molteni U, Onnela A, Peräkylä O, Piel F, Petäjä T, Praplan A P, Pringle K, Rap A, Richards N A, Riipinen I, Rissanen M P, Rondo L, Sarnela N, Schobesberger S, Scott C E, Seinfeld J H, Sipilä M, Steiner G, Stozhkov Y, Stratmann F, Tomé A, Virtanen A, Vogel A L, Wagner A C, Wagner P E, Weingartner E, Wimmer D, Winkler P M, Ye P, Zhang X, Hansel A, Dommen J, Donahue N M, Worsnop D R, Baltensperger U, Kulmala M, Carslaw K S, Curtius J (2016). Ion-induced nucleation of pure biogenic particles. Nature, 533(7604): 521–526

Knudsen M F, Riisager P (2009). Is there a link between Earth's magnetic field and low-latitude precipitation? Geology, 37(1): 71–74

Korte M, Donadini F, Constable C G (2009). Geomagnetic field for 0–3 ka: 2. A new series of time-varying global models. Geochem Geophys Geosyst, 10(6): Q06008

Laskar J, Fienga A, Gastineau M, Manche H (2011). La2010: a new orbital solution for the long-term motion of the Earth. Astron Astrophys, 532: A89

Li Z, Niu F, Fan J, Liu Y, Rosenfeld D, Ding Y (2011). Long-term impacts of aerosols on the vertical development of clouds and precipitation. Nat Geosci, 4(12): 888–894

Liu Q, Gu Z, Liu J, You H, Lü H, Chu G, Qi X, Negendank J, Mingram J, Schettler G (2005). Bulk organic carbon isotopic record of Huguangyan maar lake, southeastern China and its paleoclimatic and paleoenvironmental significance since 62 ka BP. Marine Geol & Quater Geol, 25(2): 115–126

Liu Y, Fang C, Li Q, Song H, Ta W, Zhao G, Sun C (2019). Tree-ring $\delta^{18}O$ based PDSI reconstruction in the Mt. Tianmu region since 1618 AD and its connection to the East Asian summer monsoon. Ecol Indic, 104: 636–647

Long X, Ji J, Balsam W (2011). Rainfall-dependent transformations of iron oxides in a tropical saprolite transect of Hainan Island, South China: spectral and magnetic measurements. J Geophys Res, 116(F3): F03015

Luo R, Liu Y, Zhu Q, Tang Y, Shao T (2021). Effects of aerosols on cloud and precipitation in East-Asian drylands. Int J Climatol, 41(9): 4603–4618

Nilsson A, Holme R, Korte M, Suttie N, Hill M (2014). Reconstructing Holocene geomagnetic field variation: new methods, models and implications. Geophys J Int, 198(1): 229–248

Pierce J R (2017). Cosmic rays, aerosols, clouds, and climate: recent findings from the CLOUD experiment. J Geophys Res Atmos, 122(15): 8051–8055

Pierce J R, Adams P J (2007). Efficiency of cloud condensation nuclei formation from ultrafine particles. Atmos Chem Phys, 7(5): 1367–1379

Robinson S G, Sahota J T S, Oldfield F (2000). Early diagenesis in North Atlantic abyssal plain sediments characterized by rock-magnetic and geochemical indices. Mar Geol, 163(1–4): 77–107

Robock A, Outten S (2018). Volcanoes: Role in Climate. In: Reference Module in Earth Systems and Environmental Sciences

Sato Y, Goto D, Michibata T, Suzuki K, Takemura T, Tomita H, Nakajima T (2018). Aerosol effects on cloud water amounts were successfully simulated by a global cloud-system resolving model. Nat Commun, 9(1): 985

Scheinost A C (1998). Use and limitations of second-derivative diffuse reflectance spectroscopy in the visible to near-infrared range to identify and quantify fe oxide minerals in soils. Clays Clay Miner, 46(5): 528–536

Schneider U, Becker A, Finger P, Meyer-Christoffer A, Ziese M (2018). GPCC full data monthly product version 2018 at 0.5°: monthly land-surface precipitation from rain-gauges built on GTS-based and historical data.

Schwertmann U (1988). Occurrence and formation of iron oxides in various pedoenvironments. In: Iron in Soils and Clay Minerals (pp. 267–308). New York Springer

Southon J, Kashgarian M, Fontugne M, Metivier B, Yim W W-S (2002). Marine reservoir corrections for the Indian Ocean and Southeast Asia. Radiocarbon, 44(1): 167–180

Stenchikov G (2021). The role of volcanic activity in climate and global changes. In: Letcher T M, ed. Climate Change (3rd Ed). Elsevier, 607–643

Stuiver M, Reimer P J, Reimer R W (2020). CALIB 7.1 [WWW

program] Avaible at CALIB website.

Svensmark H, Enghoff M B, Shaviv N J, Svensmark J (2017). Increased ionization supports growth of aerosols into cloud condensation nuclei. Nat Commun, 8(1): 2199

Svensmark J, Enghoff M B, Shaviv N J, Svensmark H (2016). The response of clouds and aerosols to cosmic ray decreases. J Geophys Res Space Phys, 121(9): 8152–8181

Tan L C, Cai Y J, Cheng H, Edwards L R, Gao Y L, Xu H, Zhang H, An Z (2018). Centennial- to decadal-scale monsoon precipitation variations in the upper Hanjiang River region, China over the past 6650 years. Earth Planet Sci Let, 482: 580–590

Torrent J, Barrón V (2008). Diffuse Reflectance Spectroscopy. In: Ulery A L, Richard Drees L, eds. Methods of Soil Analysis Part 5—Mineralogical Methods. Soil Sci Soc America, 367–385

Wang Q, Yang X, Anderson N J, Dong X (2016). Direct versus indirect climate controls on Holocene diatom assemblages in a sub-tropical deep, alpine lake (Lugu Hu, Yunnan, SW China). Quat Res, 86(1): 1–12

Wang Y, Cheng H, Edwards R L, He Y, Kong X, An Z, Wu J, Kelly M J, Dykoski C A, Li X (2005). The Holocene Asian monsoon: links to solar changes and North Atlantic climate. Science, 308(5723): 854–857

Williamson C J, Kupc A, Axisa D, Bilsback K R, Bui T, Campuzano-Jost P, Dollner M, Froyd K D, Hodshire A L, Jimenez J L, Kodros J K, Luo G, Murphy D M, Nault B A, Ray E A, Weinzierl B, Wilson J C, Yu F, Yu P, Pierce J R, Brock C A (2019). A large source of cloud condensation nuclei from new particle formation in the tropics. Nature, 574(7778): 399–403

Wu X, Zhang Z, Xu X, Shen J (2012). Asian summer monsoonal variations during the Holocene revealed by Huguangyan maar lake sediment record. Palaeogeogr Palaeoclimatol Palaeoecol, 323–325(15): 13–21

Xie S, Evershed R P, Huang X, Zhu Z, Pancost R D, Meyers P A, Gong L, Hu C, Huang J, Zhang S, Gu Y, Zhu J (2013). Concordant monsoon-driven postglacial hydrological changes in peat and stalagmite records and their impacts on prehistoric cultures in central China. Geology, 41(8): 827–830

Xu H, Goldsmith Y, Lan J, Tan L, Wang X, Zhou X, Cheng J, Lang Y, Liu C (2020). Juxtaposition of western Pacific subtropical high on Asian Summer Monsoon shapes subtropical East Asian precipitation. Geophys Res Let, 47(3): e2019GL084705

Yan H, Sun L, Wang Y, Huang W, Qiu S, Yang C (2011). A record of the Southern Oscillation Index for the past 2000 years from precipitation proxies. Nat Geosci, 4(9): 611–614

Yang X, Su Z, Yang J, Huang W (2012). Magnetic fabrics of maar lake sediments in tropical southern China record hydrodynamic process. Quater Sci, 32(4): 795–802

Yang X, Wei G, Yang J, Jia G, Huang C, Xie L, Huang W, Argyrios K (2014). Paleoenvironmental shifts and precipitation variations recorded in tropical maar lake sediments during the Holocene in Southern China. The Holocene, 24(10): 1216–1225

Zhang E L, Zhao C, Xue B, Liu Z H, Yu Z C, Chen R, Shen J (2017). Millennial-scale hydroclimate variations in southwest China linked to tropical Indian Ocean since the Last Glacial Maximum. Geology, 45(5): 435–438

Zhang H, Cheng H, Sinha A, Spötl C, Cai Y, Liu B, Kathayat G, Li H, Tian Y, Li Y, Zhao J, Sha L, Lu J, Meng B, Niu X, Dong X, Liang Z, Zong B, Ning Y, Lan J, Edwards R L (2021). Collapse of the Liangzhu and other Neolithic cultures in the lower Yangtze region in response to climate change. Sci Adv, 7(48): eabi9275

Zhang J, Lu H, Jia J, Shen C, Wang S, Chu G, Wang L, Cui A, Liu J, Wu N, Li F (2020a). Seasonal drought events in tropical East Asia over the last 60,000 y. Proc Natl Acad Sci USA, 117(49): 30988–30992

Zhang P, Cheng H, Edwards R L, Chen F, Wang Y, Yang X, Liu J, Tan M, Wang X, Liu J, An C, Dai Z, Zhou J, Zhang D, Jia J, Jin L, Johnson K R (2008). A test of climate, sun, and culture relationships from an 1810-year Chinese cave record. Science, 322(5903): 940–942

Zhang T, Yang X, Chen Q, Toney J L, Zhou Q, Gao H (2020b). Humidity variations spanning the 'Little Ice Age' from an upland lake in southwestern China. The Holocene, 30(2): 289–299

Zhang W, Yan H, Liu C, Cheng P, Li J, Lu F, Ma X, Dodson J, Heijnis H, Zhou W, An Z (2018). Hydrological changes in Shuangchi Lake, Hainan Island, tropical China, during the Little Ice Age. Quater Intern, 487: 54–60

Zhang Y G, Ji J F, Balsam W L, Liu L W, Chen J (2007). High resolution hematite and goethite records from ODP 1143, South China Sea: co-evolution of monsoonal precipitation and El Niño over the past 600000 years. Earth Planet Sci Let, 264(1–2): 136–150

Zhu Z, Feinberg J M, Xie S, Bourne M D, Huang C, Hu C, Cheng H (2017). Holocene ENSO-related cyclic storms recorded by magnetic minerals in speleothems of central China. Proc Natl Acad Sci USA, 114(5): 852–857